High-temperature superconductivity at the FeSe/$SrTiO_3$ interface

Yuan-Yuan Xiang,[1] Fa Wang,[2] Da Wang,[1] Qiang-Hua Wang,[1] and Dung-Hai Lee[3,4]
[1]*National Laboratory of Solid State Microstructures, Nanjing University, Nanjing 210093, China*
[2]*Department of Physics, Massachusetts Institute of Technology, Cambridge, Massachusetts 02139, USA*
[3]*Department of Physics, University of California at Berkeley, Berkeley, California 94720, USA*
[4]*Materials Sciences Division, Lawrence Berkeley National Laboratory, Berkeley, California 94720, USA*
(Received 5 June 2012; revised manuscript received 3 September 2012; published 5 October 2012)

In several recent experiments the superconducting gap of a single-unit-cell-thick FeSe film on $SrTiO_3$ substrate has been observed by scanning tunneling spectroscopy and angle-resolved photoemission spectroscopy. The value of the superconducting gap is about nine times larger than that of the bulk FeSe under ambient pressure, suggesting a much higher pairing energy scale and T_c than all other iron-based superconductors and thus calling for a better understanding of its superconducting mechanism. In this paper we study the effects of screening due to the $SrTiO_3$ ferroelectric phonons on Cooper pairing in FeSe. We conclude that it can significantly enhance the energy scale of Cooper pairing and even change the pairing symmetry. Our results also raise some concerns on whether phonons can be completely ignored for bulk iron-based superconductors.

DOI: 10.1103/PhysRevB.86.134508 PACS number(s): 74.70.Xa, 74.20.Mn, 74.20.Rp

I. INTRODUCTION

In a recent experiment[1] a single-unit-cell-thick FeSe film was grown on the TiO_2 terminated (001) surface of $SrTiO_3$(STO) by molecular beam epitaxy. Two gaps ($\sim$10 and 20 meV) were observed by scanning tunneling microscopy (STM) at low temperatures. At present there is no transport data and superconducting T_c has not been determined by resistivity measurement, but an estimate of T_c by the bulk FeSe $2\Delta/T_c$ ratio gives $T_c \sim 80$ K, which is much higher than all other iron-based superconductors.[1] Subsequently angle-resolved photoemission spectroscopy (ARPES) results reported that there are only electron Fermi surfaces in the superconducting samples,[2,3] suggesting that the superconducting FeSe films are electron doped. The ARPES-observed electron pockets are nearly circular, with an approximately constant gap on them (between 10 and 19 meV at low temperatures for different samples). By studying the temperature dependence of the energy gap in the ARPES measurement, estimates of T_c at 40–65 K are obtained.[3] Currently there is no explanation for the discrepancy of two gaps versus one gap between the STM and ARPES measurements.

The original experimental report suggested that the STO substrate plays an important role in promoting pairing in the FeSe thin films.[1] Here we recall some of the properties of STO that we think are relevant to the electron pairing problem. STO is a "quantum paraelectric" insulator.[4] The huge dielectric constant at low temperatures is due to the ionic movements. The associated phonon, the ferroelectric (FE) phonon, involve the relative displacement of the Ti and O atoms. An example of such displacement is shown in the right panel of Fig. 1. This phonon mode is soft at the zone center. This FE phonon has two important effects on the FeSe electrons. The first is to mix states separated by momentum (π,π) in the unfolded Brillouin zone. This is because a frozen FE phonon breaks the symmetry of the Fe glide plane ($z \leftrightarrow -z$ reflection about Fe plane followed by a translation to nearest-neighbor Fe), which enables the Brillouin zone unfolding. In addition, the soft zone center FE phonons can screen the intrapocket electron-electron repulsion.

At low temperatures bulk STO also undergoes an antiferrodistortive (AFD) transition. This distortion involves alternating clockwise and counterclockwise rotations of oxygen about titanium (see the left panel of Fig. 1). A recent density functional theory study[5] found that aside from zone folding, static AFD distortion has little effect on the FeSe band structure. Therefore we ignore the AFD phonon in the following discussion.

In the rest of the paper we perform a two-stage calculation to treat both the electronic correlation and the electron-phonon coupling, using the same idea of previous two-stage renormalization group (RG) studies.[6,7] The first stage is a functional renormalization group (FRG)[8,9] calculation. It determines the most important electronic scattering processes at low energies. As found in previous studies[9–11] for energies lower than the magnetic fluctuation energy scale, Λ_e, the strongest electron-electron scattering is in the Cooper channel (for superconducting samples). This is used as the input for the the second-stage analysis, in which a generalized Eliashberg equation is solved to treat the effect of FE phonons at energies lower than the maximum phonon frequency Λ_{ph} ($\Lambda_{ph} < \Lambda_e$). Some reasonable parameters are tested to see if the large T_c enhancement can be achieved. Due to the uncertainty of the surface doping we study both undoped and electron-doped FeSe.

II. THE FIRST STAGE: FRG CALCULATION

In the first stage of the calculation we employ the FRG method to derive the low-energy effective interaction at an energy cutoff Λ_e. The unrenormalized electronic Hamiltonian $H = H_{\text{band}} + H_I$ consists of the bandstructure part H_{band} and the atomic Hubbard-Hund interaction H_I. H_{band} is a tight-binding fit of ARPES-measured band structures[2] (Fig. 2). It is worth noting that this band structure differs substantially from those for other pnictides in that the hole band top near Γ and the electron band bottom near X and Y are separated by a small gap. Interestingly in a recent ARPES work on $A_xFe_ySe_2$ this feature is noted and emphasized.[12] The interaction H_I is characterized by three parameters,

 ©2012 American Physical Society

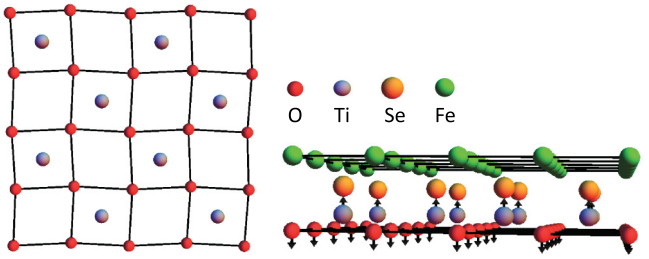

FIG. 1. (Color online) Left panel: an example of AFD distortion in the TiO_2 plane. Right panel: a caricature of the frozen FE phonon with the atomic displacement in the (001) direction.

intraorbital repulsion U, interorbital repulsion U', and Hund's interaction strength J, with the details given in Appendix A. The singular-mode FRG (SM-FRG) method used in these calculations is briefly explained in Appendix A. For all our calculations we use $(U,U',J_H) = (2,1.35,0.325)$ eV.

The FRG results are summarized in Fig. 3. For the undoped case, the leading pairing channel is $S_\pm$ with opposite signs of order parameters between electron and hole Fermi surfaces. This result is consistent with previous Fermi surface patch FRG calculations,[13] while in the electron-doped case the leading pairing channel is the fully gapped $d_{x^2-y^2}$ pairing, with opposite signs of order parameters between two electron pockets.

III. THE SECOND STAGE: THE ELIASHBERG EQUATIONS

In the first-stage calculations the electronic-correlation-driven pairing instabilities have been identified. In both undoped and electron-doped cases the leading pairing instabilities are nodeless. These are used as the input for the second-stage calculation of electron-phonon coupling effects. In this section we treat the electron-phonon coupling mainly by the phenomenological Eliashberg equation formalism. Some of our conclusions are supported by FRG calculations with electron-phonon couplings reported in Appendix B.

The formalism and notations of the Eliashberg equations closely follow those in Scalapino *et al.*[14] and McMillan.[15] The details can be found in Appendix C. In order to make analytic calculation feasible, we model the low-energy electronic degrees of freedom by two Fermi surfaces. In the case of undoped FeSe these correspond to hole and electron pockets, and for the electron-doped case both Fermi surfaces correspond to electron pockets (at X and Y). These two Fermi surfaces are

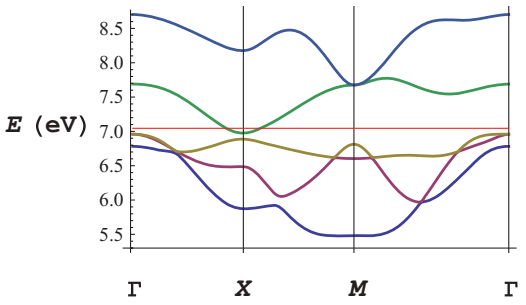

FIG. 2. (Color online) A tight-binding fit to the band dispersion observed in Ref. 2.

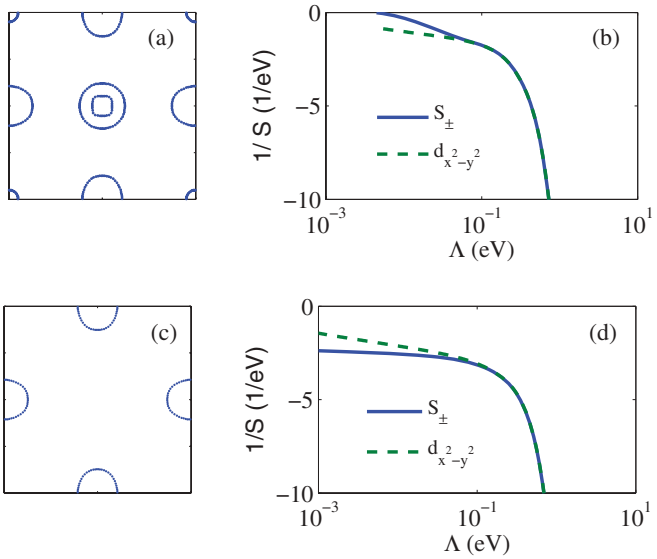

FIG. 3. (Color online) (a) and (c) Fermi surfaces of the undoped vs electron-doped FeSe band structure used in the SM-FRG calculation. (b) and (d) RG flows of the coupling strengths S of the leading pairing channels for the undoped vs electron-doped cases. Horizontal axis is the frequency cutoff Λ.

labeled by $a = 1,2$ in Eq. (C1) respectively. Moreover we assume these Fermi surfaces have constant density of states (DOS) $N_{1,2}$. Because the leading pairing instabilities driven by electronic correlations are nodeless, we ignore the dependence of the interaction vertex $V_{abcd}(\boldsymbol{p}_1,\boldsymbol{p}_2,\boldsymbol{p}_3,\boldsymbol{p}_4)$ [see Eq. (C1)] on momentum $\boldsymbol{p}_{1,2,3,4}$ and keep the dependence on the Fermi surface index only, that is, V_{abcd}. These simplifications are made in view of the presumably strong disorder-induced quasiparticle scattering at the FeSe/STO interface, which will average out the fine structures in $V_{abcd}(\boldsymbol{p}_1,\boldsymbol{p}_2,\boldsymbol{p}_3,\boldsymbol{p}_4)$ and the DOS and are consistent with the isotropic gaps observed by ARPES.[2]

Assuming the following form for the self-energy of the Nambu spinor Ψ,

$$\Sigma_a(\omega) = [1 - Z_a(\omega)]\omega\tau_0 + Z_a(\omega)\Delta_a(\omega)\tau_1, \tag{1}$$

we derive the self-consistent equations for Z and Δ following standard procedures.[14] The results are given by Eqs. (C7) and (C8) in Appendix C. Assuming the McMillan ansatz, Eqs. (C9), these equation can be solved to yield $Z_a(0) = 1 + \sum_b \sqrt{N_b/N_a}\lambda_{ab}$ for the normal state $Z_a(0)$ and the following eigenvalue problem for T_c:

$$\sum_{b=1}^{2}\lambda_{ab}\left[\ln\frac{\Lambda_{\rm ph}}{T_c}\cdot\sqrt{N_b}\Delta_b(0) + \frac{\langle\omega\rangle_{ab}}{\Lambda_{\rm ph}}\sqrt{N_b}\Delta_b(\infty)\right] + \sqrt{N_a}\Delta_a(\infty) = \sqrt{N_a}Z_a(0)\Delta_a(0) \tag{2}$$

and

$$-\sum_{b=1}^{2}v_{ab}\left[\ln\frac{\Lambda_{\rm ph}}{T_c}\sqrt{N_b}\Delta_b(0) + \ln\frac{\Lambda_{\rm e}}{\Lambda_{\rm ph}}\cdot\sqrt{N_b}\Delta_b(\infty)\right] = \sqrt{N_a}\Delta_a(\infty). \tag{3}$$

In the above equations $\lambda_{ab} = 2\int_0^\infty \frac{d\nu}{\nu}\alpha^2_{ab}(\nu)F(\nu)$, where $F(\nu)$ is the density of states associated with the phonon mode and

$\alpha^2_{ab}(\nu)$ is the effective electron-phonon coupling constants. In addition $v_{ab} = \sqrt{N_a N_b} V_{abba}$, and $\langle\omega\rangle_{ab}$ is a weighted average [weighted by $\alpha^2_{ab}(\nu)F(\nu)/\nu$] of the phonon frequency.

For the sake of simplicity we set $N_1 = N_2$, $\lambda_{aa} \to \lambda_{\text{intra}} = (\lambda_{11} + \lambda_{22})/2$, $\lambda_{ab} \to \lambda_{\text{inter}} = (\lambda_{12} + \lambda_{21})/2$, $v_{aa} \to v_{\text{intra}} = (v_{11} + v_{22})/2$, $v_{ab} \to v_{\text{inter}} = (v_{12} + v_{21})/2$, and $\langle\omega\rangle_{ab} = \langle\omega\rangle$ in the following. With the above simplifications we can determine the T_c for the "odd-sign" pairing ($\Delta_1 = -\Delta_2$) and the "even-sign" pairing ($\Delta_1 = \Delta_2$) respectively as

$$\begin{aligned} T_c^{\text{odd}} &= \Lambda_{\text{ph}} \cdot e^{-(1+\lambda_+)/\text{Max}[\lambda_- - V_-^*(1+\lambda_- \frac{\langle\omega\rangle}{\Lambda_{\text{ph}}}),0]}, \\ T_c^{\text{even}} &= \Lambda_{\text{ph}} \cdot e^{-(1+\lambda_+)/\text{Max}[\lambda_+ - V_+^*(1+\lambda_+ \frac{\langle\omega\rangle}{\Lambda_{\text{ph}}}),0]}, \end{aligned} \tag{4}$$

where

$$\begin{aligned} &\lambda_\pm = \lambda_{\text{intra}} \pm \lambda_{\text{inter}}, \quad V_\pm = V_{\text{intra}} \pm V_{\text{inter}}, \\ &V_\pm^* = V_\pm/[1 + V_\pm \ln(\Lambda_e/\Lambda_{\text{ph}})]. \end{aligned} \tag{5}$$

Note that the Max[. . . ,0] symbol is just to ensure that the denominator of the exponent is non-negative, as in the case of the Bardeen-Cooper-Schrieffer T_c formula. We have checked that changing the ratio of DOS N_1/N_2 has little effect on T_c but has a strong effect on the gap ratio Δ_1/Δ_2. In obtaining the above result we have assumed that $1 + V_\pm \ln(\Lambda_e/\Lambda_{\text{ph}}) > 0$; that is, the pure electronic driven T_c is lower than Λ_{ph}/k_B.

According to Eq. (4), increase of $\lambda_{\text{intra}} - \lambda_{\text{inter}}$ and $V_{\text{inter}} - V_{\text{intra}}$ raises the T_c for the odd-sign pairing. On the other hand, to raise the T_c of the even-sign pairing we need to increase $\lambda_{\text{intra}} + \lambda_{\text{inter}}$ but decrease $V_{\text{intra}} + V_{\text{inter}}$; that is,

$$\begin{aligned} &(\lambda_{\text{intra}} - \lambda_{\text{inter}}) \nearrow, (V_{\text{inter}} - V_{\text{intra}}) \nearrow \Rightarrow T_c^{\text{odd}} \nearrow, \\ &(\lambda_{\text{intra}} + \lambda_{\text{inter}}) \nearrow, (V_{\text{inter}} + V_{\text{intra}}) \searrow \Rightarrow T_c^{\text{even}} \nearrow. \end{aligned} \tag{6}$$

The physics behind Eq. (6) is rather simple. Odd- (even-) sign pairing *requires* the interpocket Cooper scattering to be repulsive (attractive). Since phonon-mediated scattering is necessarily attractive, it follows that strong interpocket electron-phonon interaction enhances even-sign pairing while suppress the odd-sign pairing. Because attractive intrapocket scattering strengthens both even- and odd-sign pairing, strong intrapocket electron-phonon interaction is beneficial to both.

If phonons are indeed responsible for the observed T_c enhancement, there should be other signatures of the electron-phonon coupling. For example, due to the large anharmonicity of the FE phonons, we expect using a pump laser to excite them will have a clear effect on T_c. The more traditional phonon signatures such as kink in the quasiparticle dispersion and shoulder in the tunneling experiment are discussed in Appendix D.

In the following subsections the main results for the undoped and electron-doped cases are presented. The parameters used are chosen by the following considerations: (1) Λ_e is chosen at ∼200 meV, about the typical bandwidth of spin waves in antiferromagnetic parent iron-based materials; (2) from the choice of Λ_e and the bulk FeSe T_c of ∼8 K, $V_\pm$ can be estimated to be around $1/\log(\Lambda_e/k_B T_c) \sim 0.2$; (3) the ratio $\langle\omega\rangle/\Lambda_{\text{ph}}$ is customarily chosen at 0.5; (4) the Λ_{ph} is chosen by an optimistic rough estimate of ∼100 meV, about half of Λ_e; (5) the most difficult choice is the electron-phonon coupling strength $\lambda_\pm$—we treat these as unknown parameters and draw phase diagrams with respect to them. To justify the perturbative Eliashberg equation we restrict $\lambda_{\text{inter}}, \lambda_{\text{intra}} < 1$.

A. The undoped FeSe/STO

For undoped FeSe/STO the first-stage RG generates $V_{\text{inter}} > 0$, hence favoring odd-sign (S_{+-}) pairing.[9,10,16,17] This is caused by the antiferromagnetic fluctuation. As discussed above, λ_{intra} enhances the S_{+-} pairing while λ_{inter} weakens it. Setting $V_{\text{inter}} = 0.2$ and $V_{\text{intra}} = \pm 0.05$, the "phase diagrams" as a function of λ_{intra} and λ_{inter} are shown in Figs. 4(a) and 4(b). The associated T_c enhancement factors are shown in Figs. 4(c) and 4(d). Note the magnitude of the T_c enhancement differs by approximately an order of magnitude in Figs. 4(c) and 4(d) by merely reversing the sign of V_{intra}. Clearly this quantity is not something we can confidently predict. What is robust is the fact that when $\lambda_{\text{inter}} \gg \lambda_{\text{intra}}$ electron-phonon interaction stabilizes even-sign pairing. Conversely for $\lambda_{\text{intra}} \gg \lambda_{\text{inter}}$ odd-sign pairing is favored. Since for undoped FeSe/STO the FE phonons mainly cause intrapocket electron scattering($\lambda_{\text{intra}} \gg \lambda_{\text{inter}}$), we expect the electron-phonon interaction to strengthen the odd-sign, in this case S_{+-}, pairing.

B. The electron-doped FeSe/STO

Our tight-binding fit of the ARPES band structure and the associated Fermi surfaces are shown in Fig. 2. Because the hole bands have completely sunk below the Fermi energy, the antiferromagnetic fluctuation only occurs at energies greater than the separation between the top of the hole bands and the Fermi energy. According to Ref. 2 this separation is approximately 80 meV. If sufficiently strong, this high-energy magnetic fluctuation can trigger S_{++} pairing on the electron pockets. This pairing form factor can be thought of as S_{+-} restricted to the exposed electron Fermi surfaces. When this form factor is the leading pairing channel, we expect V_{intra} and V_{inter}(between electron pockets in this case) both to be negative. Under this condition, adding the electron-phonon interaction, the phase diagram is shown in Fig. 5(a), and there is only S_{++} phase. The T_c enhancement is shown in Fig. 5(b).

For larger separation between the hole bands and E_F, the nodeless d wave (where the gap function has opposite signs on the two electron pockets) is the leading pairing channel. As pointed out in Ref. 18 in the presence of hybridization between the electron pockets (due to the absence of the $z \leftrightarrow -z$ glide plane symmetry at the interface) the d-wave pairing can become nodal. For strong hybridization the reconstructed electron pockets could have opposite sign pairing due to the repulsive electron-electron interaction.[18,19] We expect that in both cases Fig. 4 should apply; that is, sufficiently strong interpocket scattering (the first main effect of the FE phonon in earlier discussions) can destabilize the odd-sign pairing and turn it into even-sign pairing. In addition to the effect of phonon, the inevitable disorder scattering also tends to destabilize the odd-sign pairing in favor of even-sign pairing. Thus we strongly believe *the electron-doped FeSe/STO has even-sign (or S_{++}) pairing*.

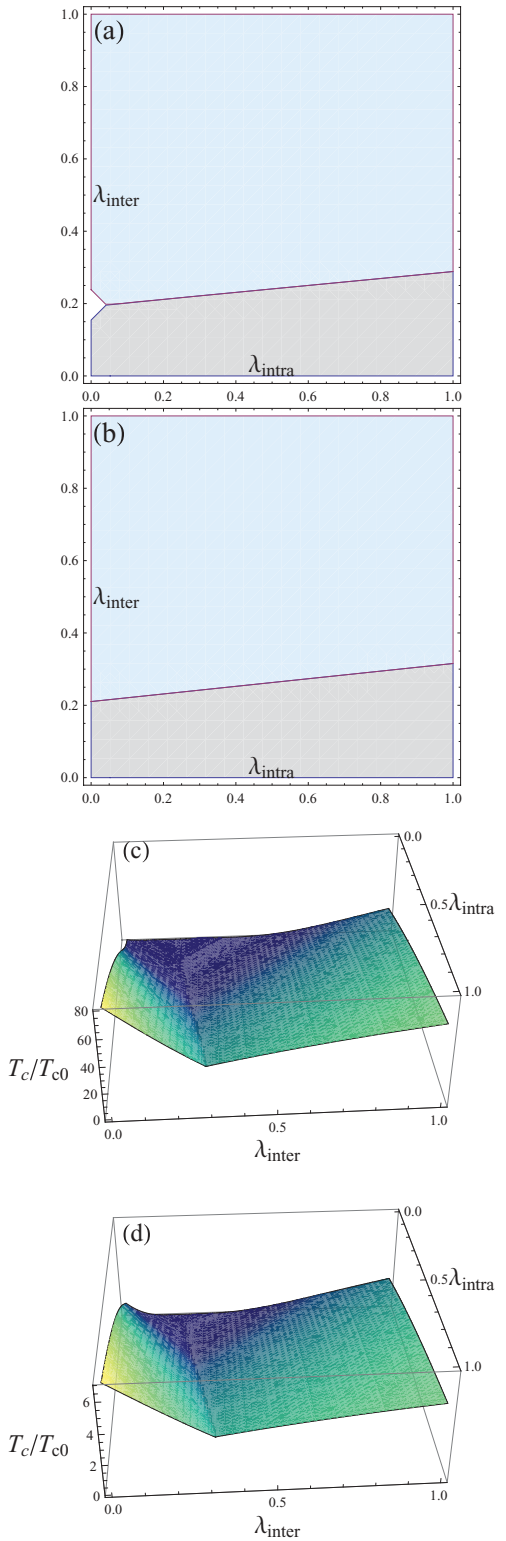

FIG. 4. (Color online) (a) and (b) The phase diagram for undoped FeSe/STO system. Light blue (gray) denotes even (odd) sign pairing, respectively. (c) and (d) The T_c enhancement factor T_c/T_{c0}, where T_{c0} is the superconducting transition temperature in the absence of the electron-phonon interaction. The parameters we used to construct the figures are $\Lambda_e/\Lambda_{ph} = 2$, $\langle\omega\rangle/\Lambda_{ph} = 0.5$, and $V_{inter} = 0.2$, $V_{intra} = 0.05$ for panels (a) and (c), and $V_{inter} = 0.2$ and $V_{intra} = -0.05$ for panels (b) and (d). The small triangular region near the lower left-hand corner of panel (a) is nonsuperconducting.

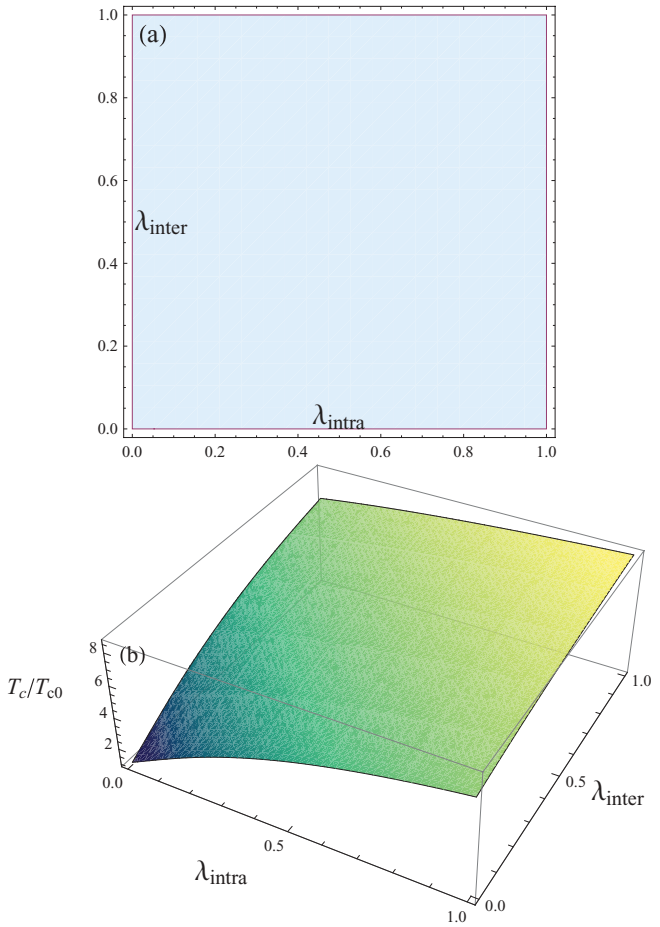

FIG. 5. (Color online) (a) The phase diagram for electron-doped FeSe/STO system. Light blue denotes the even-sign pairing. (b) The T_c enhancement factor T_c/T_{c0}, where T_{c0} is the superconducting transition temperature in the absence of the electron-phonon interaction. The parameters we used to construct the figures are $\Lambda_e/\Lambda_{ph} = 2$, $\langle\omega\rangle/\Lambda_{ph} = 0.5$, and $V_{intra} = -0.2$, $V_{inter} = -0.05$.

IV. DISCUSSION

We have studied the screening effects of the ferroelectric phonons of $SrTiO_3$ on the interaction between the electrons in FeSe, by the combination of FRG and Eliashberg equation methods. We conclude that such coupling can enhance the pairing strength of FeSe. Our results show that the T_c enhancement factor can be close to the experimental estimates of about one order of magnitude,[1] for strong electron-phonon coupling strength $\lambda \sim 1$ and reasonable values of other parameters. Moreover, we find when the interpocket electron-phonon scattering is strong, opposite-sign pairing will give way to equal-sign pairing.

Why do the FE phonons not have a similar effect on the T_c of doped STO? We believe the answer is polaron formation: For a range of strong electron-phonon coupling, the formation of polarons instead of Cooper pairs is favored. In a recent optical experiment on n-type doped STO,[20] a very sharp Drude peak with a substantial mass enhancement (consistent with that of "large polarons") was observed.

The current study raises concerns about whether the role of phonon can be completely ignored in bulk iron-based

superconductors.[21] With appropriate interpretation of λ_{intra} and λ_{inter}, our results can be used to address the phonon effects in bulk iron-based superconductors as well.

Regarding material, there are other nearly ferroelectric perovskite materials, for example, $KTaO_3$.[22] If FeSe films can be epitaxially grown on these materials, similar T_c enhancement should occur. Finally the results of Ref. 1 and the present paper suggest the . . .FeSe/$(STO)_n$/FeSe/$(STO)_n$ . . . superlattice is a promising artificial material with high T_c.

There are still many unanswered questions about these interesting experiments of FeSe thin films: (1) What caused the FeSe doping and the Se vacancy? (2) Can the discrepancy between Refs. 1 and 2 be due to surface doping caused by the sample treatment prior to the ARPES measurement? STM experiments on the annealed samples may provide very useful information for this question. (3) Are there buried, hence not yet detected, interface metallic bands?[2] (4) Are there interface ferroelectric ordering? (5) How strong is the coupling between the electrons in FeSe and the ferroelectric phonons in STO? Detailed first-principle calculations will be very useful to answer this question. (6) Why the two-unit-cell-thick (and higher thickness) FeSe films are not superconducting in the STM experiment?[1] Our current theoretical treatment ignored many possible complications indicated in these questions. Experimental clarification of these issues will greatly help the solution of the pairing mechanism in this interesting system.

ACKNOWLEDGMENTS

We are in debt to Yuan-Ming Lu, who helped us understand the phonons in $SrTiO_3$, and Fan Yang for informing us of the experimental result of Ref. 1. We thank Qi-Kun Xue and Xingjiang Zhou for sharing their unpublished results with us and R. Ramesh for telling us many important properties of $SrTiO_3$. We also thank Todadri Senthil, Tao Xiang, Jun Zhao, and Yuan Wan for helpful discussions. Q.H.W. acknowledges the support by the Ministry of Science and Technology of China (under Grants No. 2011CBA00108 and No. 2011CB922101) and NSFC (under Grants No.10974086, No. 10734120, and No. 11023002). D.H.L. acknowledges the support by DOE Grant No. DE-AC02-05CH11231.

APPENDIX A: THE SM-FRG METHOD

In this Appendix we describe the SM-FRG method used. The microscopic Hamiltonian, which is valid for all cutoff < bandwidth, that we use is $H = H_{\text{band}} + H_I + H_{\text{ph}} + H_{\text{e-ph}}$. Here H_{band} is the two-dimensional band structure. For the undoped case H_{band} is courtesy of Z.-Y. Lu.[23] For the electron-doped case it was obtained by a fit to the ARPES result.[2] H_I describes the local electron-electron interaction given by

$$\begin{aligned} H_I = {} & U \sum_{i,\alpha} n_{i,\alpha,\uparrow} n_{i,\alpha,\downarrow} + U' \sum_{i,\alpha>\beta} n_{i,\alpha} n_{i,\beta} \\ & + J_H \sum_{i,\alpha>\beta,\sigma,\sigma'} \psi^\dagger_{i,\alpha,\sigma} \psi_{i,\beta,\sigma} \psi^\dagger_{i,\beta,\sigma'} \psi_{i,\alpha,\sigma'} \\ & + J_H \sum_{i,\alpha>\beta} (\psi^\dagger_{i,\alpha,\uparrow} \psi^\dagger_{i,\alpha,\downarrow} \psi_{i,\beta,\downarrow} \psi_{i,\beta,\uparrow} + \text{H.c.}), \end{aligned} \tag{A1}$$

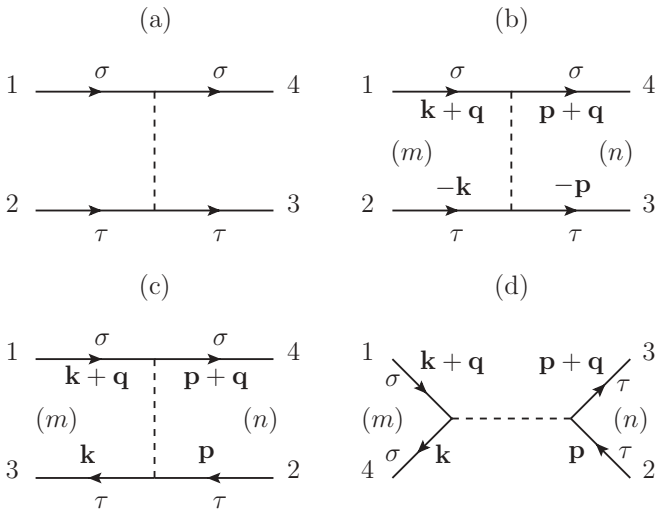

FIG. 6. A generic four-point vertex (a) is rearranged into the pairing (b), crossing (c), and direct (d) channels. Here $\mathbf{k},\mathbf{q},\mathbf{p}$ are momenta, σ and τ denote spins which are conserved during fermion propagation, and m,n denote the form factor (see the text for details).

where $\psi_{i,\alpha,\sigma}$ annihilates a spin σ electron at site i in orbital α ($\alpha = 3z^2 - r^2, xz, yz, x^2 - y^2, xy$), $n_{i,\alpha,\sigma} = \psi^\dagger_{i,\alpha,\sigma} \psi_{i,\alpha,\sigma}$, and $n_{i,\alpha} = \sum_\sigma n_{i,\alpha,\sigma}$. In the calculation of the main text we used intra-orbital repulsion $U = 2$ eV, Hund's rule coupling $J_H = 0.31$ eV, and interorbit repulsion $U' = U - 2J_H$.

Figure 6(a) shows a generic four-point vertex function Γ_{1234}, which appears in the interaction $\psi^\dagger_1 \psi^\dagger_2 (-\Gamma_{1234}) \psi_3 \psi_4$. Here 1,2,3,4 represent momentum (or real space position) and orbital label. The spins σ and τ are conserved along fermion propagators and will be suppressed henceforth. Figures 6(b)–6(d) are rearrangements of Fig. 6(a) into the pairing (P), the crossing (C), and the direct (D) channels in such a way that a collective momentum $\mathbf{q}$ can be identified. The dependence on all other momenta and orbital labels is written as

$$\begin{aligned} \Gamma^{\alpha\beta\gamma\delta}_{\mathbf{k+q},-\mathbf{k},-\mathbf{p},\mathbf{p+q}} &\to \sum_{mn} f^*_m(\mathbf{k},\alpha,\beta) P_{mn}(\mathbf{q}) f_n(\mathbf{p},\delta,\gamma), \\ \Gamma^{\alpha\beta\gamma\delta}_{\mathbf{k+q},\mathbf{p},\mathbf{k},\mathbf{p+q}} &\to \sum_{mn} f^*_m(\mathbf{k},\alpha,\gamma) C_{mn}(\mathbf{q}) f_n(\mathbf{p},\delta,\beta), \\ \Gamma^{\alpha\beta\gamma\delta}_{\mathbf{k+q},\mathbf{p},\mathbf{p+q},\mathbf{k}} &\to \sum_{mn} f^*_m(\mathbf{k},\alpha,\delta) D_{mn}(\mathbf{q}) f_n(\mathbf{p},\gamma,\beta). \end{aligned} \tag{A2}$$

Here $f_{m=(l,o)}(\mathbf{k},\alpha,\beta) = h_l(\mathbf{k}) \mathcal{M}_o(\alpha,\beta)$ is a composite form factor, where $h_l(\mathbf{k})$ is chosen from a set of orthonormal lattice harmonics and $\mathcal{M}_o$ is a matrix in the orbital basis.

The decomposition Eq. (A2) for each channel would be exact if the form factor set is complete. In practice, however, a set of a few form factors is often sufficient to capture the symmetry of the order parameters associated with leading instabilities.[24,25] In our case, the lattice harmonics are chosen as $h(\mathbf{k}) = 1$, $\cos k_x \pm \cos k_y$, $2 \cos k_x \cos k_y$, and $2 \sin k_x \sin k_y$. They are all even since only singlet pairing is relevant in our case. The $\mathcal{M}$ matrices are chosen so that the combination $\sum_{\alpha\beta} \phi_\alpha \mathcal{M}(\alpha,\beta) \phi_\beta$ (ϕ_α is the real atomic orbital function) is irreducible and transforms according to

A_{1g}, B_{1g}, or B_{2g} under the point group.[26] (One may also use any bilinear $\phi_\alpha\phi_\beta$ to determine a matrix $\mathcal{M}$, but it is less transparent symmetrywise.) Moreover, the $\mathcal{M}$ matrix is normalized as $\mathrm{Tr}\mathcal{M}^\dagger\mathcal{M} = 1$. If the total number of composite form factors is N, then P, C, and D are all $N \times N$ matrix functions of $\mathbf{q}$. Note that the P,C, and D channels are not orthogonal. The overlap between different channels are important for the growth of pairing interaction out of, for example, the magnetic interaction.[9,11,25] In the following we denote $X_K = \hat{K}X$ as the projection of X into the K channel via Eq. (A2).

In the case with electron-phonon interaction we need the phonon-mediated electron-electron scattering. According to the $H_{\mathrm{e-ph}}$ defined in the text, this vertex is given by

$$V(\mathbf{q},\nu_n) \propto \sum_{p_z} \frac{A^2}{\nu_n^2 + \omega^2(\mathbf{q} + p_z\hat{z})} \propto \frac{A^2}{\sqrt{\nu_n^2 + \omega^2(\mathbf{q})}}, \quad \text{(A3)}$$

where $\mathbf{q} = (q_x,q_y)$ and ν_n are the momentum and (Matsubara) frequency transfer in the electron-electron scattering, and the last proportionality holds to leading order in ω_0/c. The $\lambda_{\mathrm{intra,inter}}$ discussed in the main text are both proportional to A^2. Notice that this vertex is naturally in the D channel and bears trivial form factors with $h = 1$ and $\mathcal{M} = \delta_{\alpha\beta}$ since according to Eq. (B1) the electron-phonon interaction is local in real space and diagonal in orbital basis.

The partial flows of P, C, and D are given by the one-particle-irreducible diagrams shown in Fig. 7. Here the dashed line denotes four-point fermion vertex, the wavy line denotes the (surface) phonon-mediated vertex, and the dash-wavy line

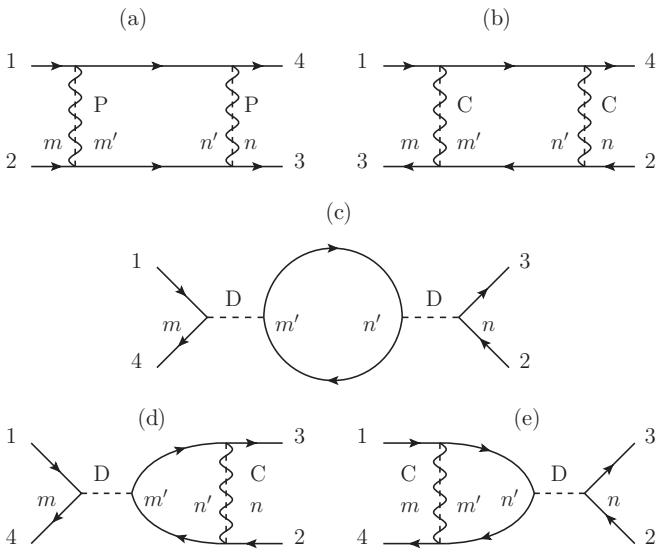

FIG. 7. One-loop diagrams contributing to the flow of the the four-point vertex function in the pairing channel (a), crossing channel (b), and direct channel [(c)–(e)]. Here m,$m'n$,n' denote form factors, while the momentum, orbital, and spin indices are left implicit. The dashed line represents the four-point fermion vertex and the dash-wavy line means that both fermion vertex and phonon propagator can be inserted separately. The diagrams are one particle irreducible with respect to both fermions and phonons, and the phonon line shares the loop frequency since external fermion fields are set at zero frequency as usual. The Matsubara frequency is continuous but subject to hard infrared cutoff at running scale Λ.

means that both types of vertices can enter. We write the partial flow equations as, in matrix form and for a collective momentum $\mathbf{q}$,

$$\begin{aligned}
\frac{\partial P}{\partial \Lambda} &= (P + V_P)\chi'_{\mathrm{pp}}(P + V_P),\\
\frac{\partial C}{\partial \Lambda} &= (C + V_C)\chi'_{\mathrm{ph}}(C + V_C),\\
\frac{\partial D}{\partial \Lambda} &= (C + V_C - D)\chi'_{\mathrm{ph}}D + D\chi'_{\mathrm{ph}}(C + V_C - D).
\end{aligned} \quad \text{(A4)}$$

Here Λ is the running Matsubara frequency cutoff, V_K is the phonon-mediated interaction projected into the K channel at cutoff Λ, and $\chi'_{\mathrm{pp/ph}}$ are matrix kernels with elements

$$\begin{aligned}
(\chi'_{\mathrm{pp}})_{mn} &= -\frac{1}{2\pi}\int \frac{d^2\mathbf{p}}{(2\pi)^2} f_m(\mathbf{p},\alpha,\beta)G_{\alpha\gamma}(\mathbf{p}+\mathbf{q},i\Lambda)\\
&\quad \times G_{\beta\delta}(-\mathbf{p},-i\Lambda)f_n^*(\mathbf{p},\gamma,\delta) \ + (\Lambda \to -\Lambda),\\
(\chi'_{\mathrm{ph}})_{mn} &= -\frac{1}{2\pi}\int \frac{d^2\mathbf{p}}{(2\pi)^2} f_m(\mathbf{p},\alpha,\beta)G_{\alpha\gamma}(\mathbf{p}+\mathbf{q},i\Lambda)\\
&\quad \times G_{\delta\beta}(\mathbf{p},i\Lambda)f_n^*(\mathbf{p},\gamma,\delta) \ + (\Lambda \to -\Lambda),
\end{aligned} \quad \text{(A5)}$$

where G is the bare fermion propagator in the orbital basis and the summation over orbitals is left implicit.

Clearly, because of the Λ dependence, the effect of phonon-mediated interaction, V, is important only if Λ reaches the phonon band, above which the main contribution to the flow of the fermion interaction vertex is from pure electron-electron interaction. However, the electronic excitations do modify phonon self-energy and electron-phonon vertex even when the cutoff scale is above the phonon bandwidth. In the present work such effects are accounted for by using the experimentally measured phonon dispersion and the electron-phonon coupling constant. The flows in Eq. (A4) collect contributions from independent one-particle-irreducible diagrams for the total change $d\Gamma$, which need to be subsequently projected to the three channels. Therefore, the full flow equations can be formally written as

$$\frac{dK}{d\Lambda} = \frac{\partial K}{\partial \Lambda} + \hat{K}\sum_{K'\neq K}\frac{\partial K'}{\partial \Lambda}, \quad \text{(A6)}$$

for $K = P,C$, and D. We used the fact that $\hat{K}\partial K = \partial K$ by definition.

The functions P, C, and D are related to the effective interactions as $V_{\mathrm{SC}} = -P - V_P$ in SC channels, $V_{\mathrm{SDW}} = C + V_C$ in SDW channels, and $V_{\mathrm{CDW}} = C + V_C - 2D$ in CDW channels. We monitor the most negative singular values $S_{\mathrm{SC,SDW,CDW}}$ of such interactions (for all $\mathbf{q}$) versus the running cutoff Λ. The most negative one among $S_{\mathrm{SC,SDW,CDW}}$ tells us which channel is becoming unstable. The associated eigenfunction dictates the symmetry and wave vector of the order parameter.

APPENDIX B: FRG CALCULATION WITH ELECTRON-PHONON COUPLING

In this Appendix we report our FRG calculation results for undoped FeSe with electron-phonon coupling. The phonon

Hamiltonian is given by $H_{\rm ph} = \sum_{\mathbf{p}} \omega(\mathbf{p}) a^\dagger_{\mathbf{p}} a_{\mathbf{p}}$. Here $\mathbf{p}$ is the three-dimensional momentum. We assume the following dispersion for the FE phonon $\omega(\mathbf{p}) = \sqrt{\omega_0^2 + c^2 p^2}$ where $\omega_0 \approx 2$ meV and $c \sim 70$ meV Å are estimated from an early neutron measurement.[27] The electron-phonon Hamiltonian is given by

$$H_{\rm e-ph} = A \sum_{i,\alpha} u_i n_{i\alpha} \to \sum_{p_z} \sum_{\mathbf{k}a,\mathbf{k}'b} g_{\mathbf{k}a,\mathbf{k}'b;p_z} \times \left(a^\dagger_{\mathbf{k}-\mathbf{k}'+\mathbf{p}_z} + a_{\mathbf{k}'-\mathbf{k}-\mathbf{p}_z}\right) \Psi^\dagger_{\mathbf{k}'b} \tau_3 \Psi_{\mathbf{k}a}. \quad \text{(B1)}$$

$H_{\rm e-ph}$ describes the coupling between electrons in the FeSe layer and the nearest ion displacement u_i in the TiO_2 layer of STO. In the above $\mathbf{p}_z = p_z \hat{z}$ is the out-of-plane momentum of the phonon and τ_3 is the third Pauli matrix in the Nambu space. The summation over p_z follows from the fact that the electron-phonon coupling occurs at the interface. Here a and b label the electron bands, and $g_{\mathbf{k}a,\mathbf{k}'b;p_z} \propto A\langle \mathbf{k}a|\mathbf{k}'b\rangle / \sqrt{\omega(\mathbf{k}-\mathbf{k}'+\mathbf{p}_z)}$, where $\langle \mathbf{k}a|\mathbf{k}'b\rangle$ is the overlap between band Bloch states. The phonon-mediated intra- and interpocket Cooper scattering strengths are given by $\lambda_{\rm intra} = \sum_{a=1}^{5} \lambda_{aa}/5$ and $\lambda_{\rm inter} = \sum_{a\neq b} \lambda_{ab}/20$, where

$$\lambda_{ab} = \sqrt{N_a N_b} \sum_{p_z} \left\langle\!\!\left\langle \frac{2\left|g_{\mathbf{k}a,\mathbf{k}'b;p_z}\right|^2}{\omega(\mathbf{k}-\mathbf{k}'+\mathbf{p}_z)} \right\rangle\!\!\right\rangle_{a,b}, \quad \text{(B2)}$$

where $\langle\langle\cdot\rangle\rangle$ denotes the joint average over $\mathbf{k}$ and $\mathbf{k}'$, which lie on Fermi pockets a and b respectively. Using ω_0 and c above and the Fermi pockets in Fig. 8(a) we estimate $\lambda_{\rm inter}/\lambda_{\rm intra} \sim 1/12$.

We generalize the SM-FRG method[24,25] to treat the effects of both electron-electron and electron-phonon interactions. In principle, we envision a boson-fermion FRG calculation that involves the flow of electron self-energy, the phonon self-energy, the electron-phonon coupling vertex, the four-point phonon vertex, and the electron-electron interaction vertex. However, in the following we view the electron dispersion, the phonon dispersion, and the electron-phonon coupling as fully renormalized quantities. The first two can be determined from experiments and the last quantity is viewed as an adjustable parameter in our theory. The RG flow of the electron-electron interaction, including contributions from the pure electron-electron interaction and the phonon-mediated interaction, is left. In the following the renormalized interactions in the superconducting (SC) and spin density wave (SDW) channels are denoted as $S_{\rm SC,SDW}$. (The charge density wave channel turns out to be unimportant and is not discussed.) The definitions as well as technical details of the SM-FRG method can be found in Appendix A.

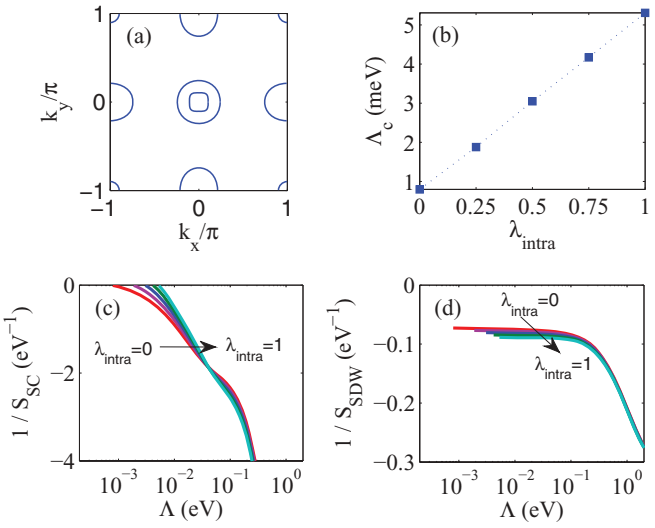

FIG. 8. (Color online) (a) Undoped FeSe Fermi surface(s). (b) The superconducting critical scale Λ_c vs $\lambda_{\rm intra}$. Panels (c) and (d) presents the flow of $S_{\rm SC}$ and $S_{\rm SDW}$, respectively. (Higher scales are not shown.) The value of $\lambda_{\rm intra}$ increases by equal intervals along the arrows.

Figure 8(b) summarizes the superconducting critical scale Λ_c (filled squares) versus the electron-phonon interaction parameter $\lambda_{\rm intra}$ ($\lambda_{\rm inter} \sim \lambda_{\rm intra}/12$). This is extracted from Fig. 8(c), which shows the flow of $S_{\rm SC}$. Figure 8(b) shows a linearly rising Λ_c as a function of $\lambda_{\rm intra}$. When we compare the maximum Λ_c with that in the absence of electron-phonon interaction, a maximum T_c enhancement ~6.5 is obtained. Given the fact that $\lambda_{\rm intra} \sim 12\lambda_{\rm inter}$ this result is consistent with Fig. 4. We have checked that for all values of $\lambda_{\rm intra}$ in Fig. 8(c) the pairing symmetry remains S_{+-}. Figure 8(d) shows that the $S_{\rm SDW}$ almost saturates at low energy scales, and the electron-phonon coupling reduces $1/S_{\rm SDW}$ only slightly. Since this type of SDW is related to the pairing interaction, the above observation justifies our previous assumptions for the input to the Eliashberg calculation.

APPENDIX C: MULTIPLE-BAND ELIASHBERG EQUATION

In this Appendix we briefly outline the derivation of the multiple-band Eliashberg equations following the single-band case of Scalapino *et al.*.[14]

The effective electron-phonon Hamiltonian we consider, at the energy cutoff $\Lambda_{\rm e}$, is given by

$$H = \sum_{a=1}^{2} \sum_{\boldsymbol{p}} \epsilon_{\boldsymbol{p}a} \Psi^\dagger_{\boldsymbol{p}a} \tau_3 \Psi_{\boldsymbol{p}a} + \sum_{\boldsymbol{q}} \omega(\boldsymbol{q}) a^\dagger_{\boldsymbol{q}} a_{\boldsymbol{q}} + \sum_{a,b} \sum_{\boldsymbol{p},\boldsymbol{p}'} g_{\boldsymbol{p}\boldsymbol{p}',ab} \varphi_{\boldsymbol{p}-\boldsymbol{p}'} \Psi^\dagger_{\boldsymbol{p}'b} \tau_3 \Psi_{\boldsymbol{p}a} + \frac{1}{2} \sum_{a,b,c,d} \sum_{\boldsymbol{p}_1,\boldsymbol{p}_2,\boldsymbol{p}_3} V_{abcd}(\boldsymbol{p}_1,\boldsymbol{p}_2,\boldsymbol{p}_3,\boldsymbol{p}_4) \times \left(\Psi^\dagger_{\boldsymbol{p}_3 c} \tau_3 \Psi_{\boldsymbol{p}_1 a}\right)\left(\Psi^\dagger_{\boldsymbol{p}_4 d} \tau_3 \Psi_{\boldsymbol{p}_2 b}\right). \quad \text{(C1)}$$

Here $\Lambda_{\rm e}$ is much smaller than the bandwidth but larger than maximal phonon frequency $\Lambda_{\rm ph}$, $\Psi_{\boldsymbol{p}a}$ is the Nambu spinor for electron band a with dispersion $\epsilon_{\boldsymbol{p}a}$, $a_{\boldsymbol{q}}$ is the destruction operator for phonon with dispersion $\omega(\boldsymbol{q})$, $\varphi_{\boldsymbol{q}} = a^\dagger_{\boldsymbol{q}} + a_{-\boldsymbol{q}}$, $\boldsymbol{p}_4 = \boldsymbol{p}_1 + \boldsymbol{p}_2 - \boldsymbol{p}_3$, τ_3 is the Pauli matrix, and $V_{abcd}(\boldsymbol{p}_1,\boldsymbol{p}_2,\boldsymbol{p}_3,\boldsymbol{p}_4)$ is the (effective) electron-electron interaction. Different levels of simplification are applied to Eq. (C1), which is discussed in more details in the following.

Assume the Green's function of Nambu spinor Ψ to be given by

$$[G_a(\boldsymbol{p},\omega)]^{-1} = \omega - \epsilon_{\boldsymbol{p}a}\tau_3 - \Sigma_a(\boldsymbol{p},\omega). \quad \text{(C2)}$$

The self-consistent equation of the self-energy $\Sigma_a(\boldsymbol{p},\omega)$ is

$$\Sigma_a(\boldsymbol{p},i\omega) = -T\sum_{\omega',\boldsymbol{p}'}\sum_b \tau_3 G_b(\boldsymbol{p}',i\omega')\tau_3\cdot[|g_{\boldsymbol{p}\boldsymbol{p}',ab}|^2 D(\boldsymbol{p}-\boldsymbol{p}',i\omega-i\omega') + V_{abba}(\boldsymbol{p},\boldsymbol{p}',\boldsymbol{p}',\boldsymbol{p})], \tag{C3}$$

where ω' is fermion Matsubara frequency. $D(\boldsymbol{q},\nu)$ is the Green's function of the phonon. Using the spectral representation

$$D(\boldsymbol{q},i\nu') = \int_0^\infty d\nu\, B(\boldsymbol{q},\nu)\left[\frac{1}{i\nu'-\nu} - \frac{1}{i\nu'+\nu}\right], \tag{C4}$$

and summing over ω' by the procedure of Ref. 14, the self-consistent equation becomes

$$\Sigma_a(\boldsymbol{p},\omega) = -\sum_b \frac{1}{\pi}\sum_{\boldsymbol{p}'}\int_{-\infty}^{\infty} d\omega''\,\mathrm{Im}[\tau_3 G_b(\boldsymbol{p}',\omega'')\tau_3]|g_{\boldsymbol{p}\boldsymbol{p}',ab}|^2\int_0^\infty d\nu\, B(\boldsymbol{p}-\boldsymbol{p}',\nu)\left[\frac{N(\nu)+f(-\omega'')}{\omega-\omega''-\nu}+\frac{N(\nu)+f(\omega'')}{\omega-\omega''+\nu}\right]$$
$$-\sum_b \frac{1}{\pi}\sum_{\boldsymbol{p}'}\int_{-\infty}^{+\infty} d\omega''\,\mathrm{Im}[\tau_3 G_b(\boldsymbol{p}',\omega'')\tau_3]\frac{1}{2}V_{abba}(\boldsymbol{p}-\boldsymbol{p}')\tanh(\beta\omega''/2). \tag{C5}$$

Assume each electron band a has a circular Fermi surface with constant DOS N_a, define $\alpha^2_{ab}(\nu)F(\nu)$ as the average of $\sqrt{N_a N_b}|g_{\boldsymbol{p}\boldsymbol{p}',ab}|^2 B(\boldsymbol{p}-\boldsymbol{p}',\nu)$ over $\boldsymbol{p}$ on Fermi surface a and $\boldsymbol{p}'$ on Fermi surface b, and ignore the momentum dependence of Σ close to Fermi surface. This equation further simplifies to

$$\sqrt{N_a}\Sigma_a(\omega) = \sum_b \sqrt{N_b}\int_{-\Lambda_e}^{\Lambda_e} d\epsilon_{\boldsymbol{p}',b}\left\{-\frac{1}{\pi}\int_{-\infty}^{\infty} d\omega''\int_0^\infty d\nu\,\alpha^2_{ab}(\nu)F(\nu)\mathrm{Im}[\tau_3 G_b(p',\omega'')\tau_3]\left[\frac{N(\nu)+f(-\omega'')}{\omega-\omega''-\nu}+\frac{N(\nu)+f(\omega'')}{\omega-\omega''+\nu}\right]\right.$$
$$\left.-\frac{1}{\pi}\int_{-\infty}^{+\infty} d\omega''\,\mathrm{Im}[\tau_3 G_b(p',\omega'')\tau_3]\frac{1}{2}v_{ab}\tanh(\beta\omega''/2)\right\}. \tag{C6}$$

Here $N(\nu)=1/(e^{\beta\nu}-1)$ and $f(\omega)=1/(e^{\beta\omega}+1)$ are the Bose and Fermi distribution functions, $v_{ab}=\sqrt{N_a N_b}V_{abba}$. Assuming that Σ_a takes the form of Eq. (1), the above equation reduces to

$$\sqrt{N_a}[1-Z_a(\omega)] = \sum_b \sqrt{N_b}\int_0^\infty d\nu\,\alpha^2_{ab}(\nu)F(\nu)\int_0^{\Lambda_e} d\omega'\,\mathrm{Re}\left[\frac{\omega'}{\sqrt{\omega'^2-\Delta_b^2(\omega')}}\right]2\left[\frac{N(\nu)+f(-\omega')}{\omega^2-(\omega'+\nu)^2}+\frac{N(\nu)+f(\omega')}{\omega^2-(\omega'-\nu)^2}\right], \tag{C7}$$

and

$$\sqrt{N_a}Z_a(\omega)\Delta_a(\omega) = -\sum_b \sqrt{N_b}\int_0^\infty d\nu\,\alpha^2_{ab}(\nu)F(\nu)\int_0^{\Lambda_e} d\omega'\,\mathrm{Re}\left[\frac{\Delta_b(\omega')}{\sqrt{\omega'^2-\Delta_b^2(\omega')}}\right]2\left[\frac{(\omega'+\nu)[N(\nu)+f(-\omega')]}{\omega^2-(\omega'+\nu)^2}\right.$$
$$\left.+\frac{(\omega'-\nu)[N(\nu)+f(\omega')]}{\omega^2-(\omega'-\nu)^2}\right]-\sum_b\sqrt{N_b}\int_0^{\Lambda_e} d\omega'\,\mathrm{Re}\left[\frac{\Delta_b(\omega')}{\sqrt{\omega'^2-\Delta_b^2(\omega')}}\right]v_{ab}\tanh(\beta\omega'/2). \tag{C8}$$

These equations can be solved numerically for the frequency dependence of Z and Δ. For a more transparent demonstration of the physics, we adopt the McMillan approximation[15] and look for solutions of the form

$$\begin{aligned} &Z_a(\omega<\Lambda_{\mathrm{ph}}) = Z_a(0), \quad Z_a(\omega>\Lambda_{\mathrm{ph}}) = 1,\\ &\Delta_a(\omega<\Lambda_{\mathrm{ph}}) = \Delta_a(0), \quad \Delta_a(\omega>\Lambda_{\mathrm{ph}}) = \Delta_a(\infty). \end{aligned} \tag{C9}$$

This leads to the generalized McMillan formula (3) in the main text.

APPENDIX D: THE SIGNATURES OF ELECTRON-PHONON COUPLING

Conventional signatures of the electron-phonon interaction include the phonon-induced kink in the normal-state dispersion and the phonon shoulder in the tunneling spectra. However, these features are most pronounced when $\alpha^2(\nu)F(\nu)$ have a sharp peak at a characteristic phonon frequency. While this is indeed the case for Einstein phonons, it is not true for the soft phonons under discussion. Here we expect $\alpha^2(\nu)F(\nu)$ to have a wide distribution. Therefore, the above phonon features may not be very obvious. For example, using the parameters described in Appendix B a typical renormalized quasiparticle dispersion in the normal state near the Fermi surface is shown in Fig. 9.

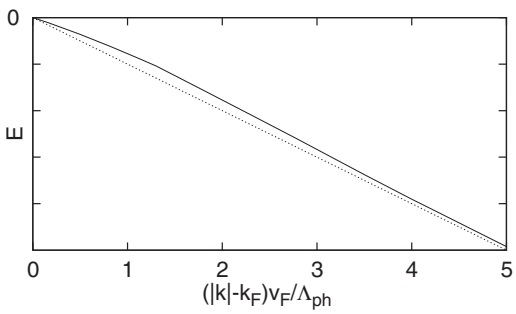

FIG. 9. Solid (dashed) line is the renormalized (unrenormalized) electron dispersion, obtained by numerical solution of Eq. (C7) with parameters $\lambda_{\mathrm{intra}}=0.5$ and $\lambda_{\mathrm{inter}}=0$, and the model of FE phonon described in Sec. II. No prominent kink is visible despite significant (factor 1.5) mass enhancement at the Fermi level.

[1]Q.-Y. Wang *et al*., Chin. Phys. Lett. **29**, 037402 (2012).
[2]D. Liu *et al*., Nat. Commun. **3**, 931 (2012).
[3]S. He *et al*., arXiv:1207.6823 (unpublished).
[4]K. A. Müller and H. Burkard, Phys. Rev. B **19**, 3593 (1979).
[5]K. Liu, Z.-Y. Lu, and T. Xiang, Phys. Rev. B **85**, 235123 (2012).
[6]G. T. Zimanyi, S. A. Kivelson, and A. Luther, Phys. Rev. Lett. **60**, 2089 (1988).
[7]H. Fu, C. Honerkamp, and D.-H. Lee, Europhys. Lett. **76**, 146 (2006).
[8]C. Honerkamp, M. Salmhofer, N. Furukawa, and T. M. Rice, Phys. Rev. B **63**, 035109 (2001).
[9]F. Wang, H. Zhai, Y. Ran, A. Vishwanath, and D.-H. Lee, Phys. Rev. Lett. **102**, 047005 (2009); F. Wang, H. Zhai, and D.-H. Lee, Europhys. Lett. **85**, 37005 (2009).
[10]A. V. Chubukov, D. V. Efremov, and I. Eremin, Phys. Rev. B **78**, 134512 (2008).
[11]For a recent review of theoretical studies of the pairing mechanism in the iron-based superconductors, see F. Wang and D.-H. Lee, Science **332**, 200 (2011).
[12]F. Chen, M. Xu, Q. Q. Ge, Y. Zhang, Z. R. Ye, L. X. Yang, Juan Jiang, B. P. Xie, R. C. Che, M. Zhang, A. F. Wang, X. H. Chen, D. W. Shen, X. M. Xie, M. H. Jiang, J. P. Hu, and D. L. Feng, Phys. Rev. X **1**, 021020 (2011).
[13]F. Wang, H. Zhai, and D.-H. Lee, Phys. Rev. B **81**, 184512 (2010).
[14]D. J. Scalapino, J. R. Schrieffer, and J. W. Wilkins, Phys. Rev. **148**, 263 (1966).
[15]W. L. McMillan, Phys. Rev. **167**, 331 (1968).
[16]I. I. Mazin, D. J. Singh, M. D. Johannes, and M. H. Du, Phys. Rev. Lett. **101**, 057003 (2008)
[17]K. Kuroki, S. Onari, R. Arita, H. Usui, Y. Tanaka, H. Kontani, and H. Aoki, Phys. Rev. Lett. **101**, 087004 (2008).
[18]I. I. Mazin, Phys. Rev. B **84**, 024529 (2011).
[19]M. Khodas and A. V. Chubukov, Phys. Rev. Lett. **108**, 247003 (2012).
[20]J. L. M. van Mechelen, D. van der Marel, C. Grimaldi, A. B. Kuzmenko, N. P. Armitage, N. Reyren, H. Hagemann, and I. I. Mazin, Phys. Rev. Lett. **100**, 226403 (2008).
[21]This issue has been raised in H. Kontani and S. Onari, Phys. Rev. Lett. **104**, 157001 (2010).
[22]C. H. Perry and T. F. McNelly, Phys. Rev. **154**, 456 (1967); C. H. Perry, R. Currat, H. Buhay, R. M. Migoni, W. G. Stirling, and J. D. Axe, Phys. Rev. B**39**, 8666 (1989).
[23]Z.-Y. Lu (private communication).
[24]C. Husemann and M. Salmhofer, Phys. Rev. B **79**, 195125 (2009).
[25]W.-S. Wang, Y.-Y. Xiang, Q.-H. Wang, F. Wang, F. Yang, and D.-H. Lee, Phys. Rev. B **85**, 035414 (2012).
[26]Y. Wan and Q.-H. Wang, Europhys. Lett. **85**, 57007 (2009). In this paper symmetries of bilinears involving xz and yz orbitals are considered, but extension to five orbitals is straightforward.
[27]Y. Yamada and G. Shirane, J. Phys. Soc. Jpn. **26**, 396 (1969).